Water striders are impervious to raindrop collision forces and submerged by collapsing craters

Daren A. Watson[a,1] (ID), Mason R. Thornton[b], Hiba A. Khan[b], Ryan C. Diamco[b], Duygu Yilmaz-Aydin[c], and Andrew K. Dickerson[d,1,2] (ID)

Water striders are abundant in areas with high humidity and rainfall. Raindrops can weigh more than 40 times the adult water strider and some pelagic species spend their entire lives at sea, never contacting ground. Until now, researchers have not systematically investigated the survival of water striders when impacted by raindrops. In this experimental study, we use high-speed videography to film drop impacts on water striders. Drops force the insects subsurface upon direct contact. As the ensuing crater rebounds upward, the water strider is propelled airborne by a Worthington jet, herein called the first jet. We show the water strider's locomotive responses, low density, resistance to wetting when briefly submerged, and ability to regain a super-surface rest state, rendering it impervious to the initial impact. When pulled subsurface during a second crater formation caused by the collapsing first jet, water striders face the possibility of ejection above the surface or submersion below the surface, a fate determined by their position in the second crater. We identify a critical crater collapse acceleration threshold ~ 5.7 gravities for the collapsing second crater which determines the ejection and submersion of passive water striders. Entrapment by submersion makes the water strider poised to penetrate the air–water interface from below, which appears impossible without the aid of a plastron and proper locomotive techniques. Our study is likely the first to consider second crater dynamics and our results translate to the submersion dynamics of other passively floating particles such as millimetric microplastics atop the world's oceans.

impact craters | jets | rainfall | insects | splash

Water striders dwell and locomote atop the free surface of Earth's marine ecosystems and are the only insect group capable of completing a full life cycle in an aquatic environment (Fig. 1A) (1–7). Marine environments experience some of the most violent storms on Earth, resulting in surface perturbations that generate ripples and splashes, exposing water striders to the threats of saturation and submersion (8–10). The reaction of water striders to surface perturbation has been studied with respect to escape jumping atop deep liquid pools, but responses to direct impacts by drops are not yet understood (11–15). Rain consisting of water drops with diameter D = 0.6 to 5 mm, mass m = 0.11 to 65 mg, and terminal velocity U = 6 to 9 m/s, is likely perceived by the water strider as the periodic deformation of a liquid surface (16, 17) when striders are fortunate enough to not be bludgeoned by oncoming drops (18, 19), as those shown in Fig. 1B and Movie S1. In this experimental study, we systematically investigate how such small, aquatic-dwelling creatures survive the onslaught of impacting drops. We fix drop diameter D = 4.0 mm ± 0.2 mm near the high end of natural drop size and larger than most measurable rain (16, 20). Raindrops of this size have a terminal velocity (20, 21) of 8.89 m/s. In the laboratory, we are able to generate impact velocities up to 68% of terminal, $U = (2gH)^{1/2}$ = 2.2 to 6.0 m/s, producing Froude numbers in the range Fr = U^2/gD = 127 to 850, where g = 9.81 m/s² is the acceleration due to gravity and H = 0.3 to 1.7 m are the drop heights. We note that our choice of H is constrained by the height restriction of an in-lab rain simulator (20). However, in the range of Froude numbers on test, impacts create energetic craters and Worthington jets (22), and impacts are dominated by drop inertia rather than gravity. In contrast to energetic drops, resting striders have a body mass M = 0.83 mg ± 0.17 mg number of striders N = 5, 2nd nymphal instar (8), and M = 6.44 mg ± 1.50 mg (N = 5, adults). The mass ratios of impacting drops on test to water striders, $m^* = m/M \approx 41$ for the 2nd nymphal instars, and $m^* = m/M \approx 5$ for adults, where mass of spherical drops is $m = \rho\pi D^3/6$ = 33.5 mg and ρ = 999 kg/m³ is the density of water, suggest that striders are at risk during drop collisions. We herein address the forces and phases of impact these large drops create, and address the increased danger between our

Significance

The familiar water strider has received intrigue for its unique locomotion; this study considers their fate in the face of energetic raindrop impacts. We identify a seemingly ignored drop impact feature, a second crater, formed following descent of the rebounding jet, whose retraction produces a water surface acceleration strong enough to leave the water strider below the surface, submerged. We reveal the morphological features that enable striders to survive the onslaught of violent rainfall that, in addition to superhydrophobicity, include passivity and the ability to resurface by swimming. Over the timescales of impact, striders and plastics of comparable size are nearly indistinguishable. Our results lay a foundation for the transport of other floating debris subsurface.
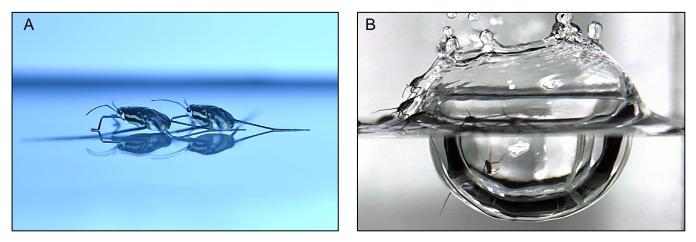
Fig. 1. (*A*) *Trepobates subnitidus* water striders resting atop the free surface of a liquid bath. (*B*) Water striders entrained subsurface during crater formation and dispersed with the ascending splash crown after drop impact. Corresponding video is Movie S1.

drops and terminal drops of the same size, elucidating the robustness of water striders to adverse super-surface conditions during rainfall.

Free-falling drops striking an aqueous pool of similar liquid properties create a splash at sufficiently large impact velocities (23–29) (Movie S2). Drops coalesce with the liquid bath when gently deposited onto the free surface, when the impact Weber number $We = \rho U^2 D/\sigma \lesssim 81$, while for increasing velocities U, drops create craters (30) followed by the propulsion of super-surface axisymmetric jets that subsequently break up into secondary droplets due to Rayleigh-Plateau instabilities (27–29, 31–36). The evolution of impact not only rapidly relocates striders but presents interface shapes that starkly contrast that of a quiescent or moderately disturbed free surface.

Under "normal" conditions, super-surface dwelling is supported by surface tension with the Baudoin number (6) $Ba = Mg/\sigma\ell \ll 1$, where $\sigma = 72$ mN/m is the surface tension of water, and $\ell \approx 5$ mm is the surface tension length of all the legs (7, 37) shown in Fig. 2*A*. Microscopic hairs on the strider legs as shown in Fig. 2*B* permit superhydrophobicity and free surface support (7, 38–45) and detect surface vibrations (46). Similarly, the exoskeleton (39) (Fig. 2 *C* and *D*) is populated with both micro-(1.5 to 2.0 μm in long, ~1 μm wide) and macro-(40 to 60 μm long, 3 μm wide) hairs such that water contact angle (7, 44) exceeds 150°. The surface-tension-driven interaction between water striders and the free surface suggests that members of this insect group can withstand multiple times their own body weight without compromising the insects' position atop aqueous habitats. In this study, we show how the water strider's superhydrophobic exoskeleton protects the insect during rainfall impacts and subsurface transport.

While the fate of flying insects in rainfall has been studied (18, 19), we here provide the first documented investigation on the physics involved in the splashing of semi-aquatic insects atop deep liquid pools. The brief timescale of impact ensures that a water strider is functionally passive. Therefore, our results apply to the surface transport of similarly sized passive particles, such as the floating plastics plaguing our world's oceans (47–49). The only study of raindrop impact on microplastics considers the aerosolization of those a few tens of microns in size much smaller than our millimetric striders (20). Droplets ejected during impact are capable of carrying microscale particles skyward.

Results

The water entry of raindrops can be summarized in stages as illustrated in Fig. 3, namely: drop collision with the free surface; air entrainment and splash crown ascension, crater collapse and Worthington jet projection; and jet collapse forming a second crater. In this study, the ability of water striders to survive impacts by raindrops is tested. We populate the free surface of a deep liquid pool with water striders and observe splashes created by impacting drops from various heights in the range $H = 0.3$ to 1.7 m. Water striders survive drop collisions despite their rapid displacement above and below the free surface.

The likelihood of raindrop impacts on striders during a rainfall event can be predicted by considering the plan view area of the insects as seen by a falling raindrop. A depiction of the impact area assessment is shown in Fig. 2*A*, where the red area highlights direct strider contact with a 3-mm diameter drop. As such, collisions within the proximity of the impact area are classified as direct impacts. Drops fall too rapidly to elicit any evasive response
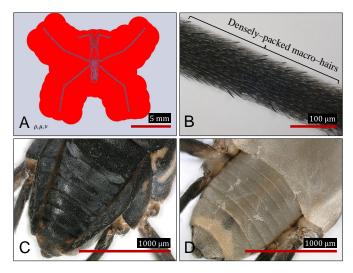

Fig. 2. (*A*) Impact area of adult water strider. Microscopic images showing (*B*) densely–packed macrohairs along the leg of the water strider, and the (*C*) dorsal, and (*D*) ventral views of an adult's exoskeleton. The exoskeleton is populated with both micro- and macro-hairs such that the water contact angle exceeds 150°.
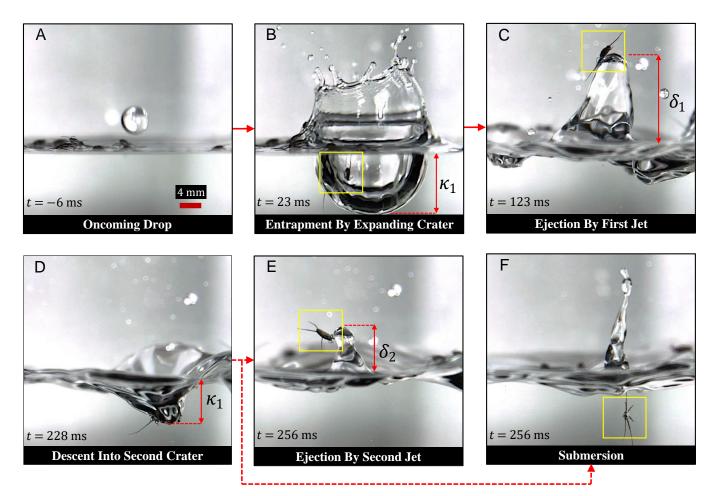
Fig. 3. (*A*) Free falling drop prior to water entry. (*B*) Drop transports water strider below the free surface during crater expansion. (*C*) The first jet propels the water strider above the free surface following crater collapse. (*D*) Water strider entrapped below the free surface during second crater formation. The entrapped insect is either (*E*) ejected or (*F*) submerged following the collapse of the second crater. We choose the free surface as $\kappa_1 = \delta_1 = 0$ cm, where κ_1 and δ_1 are the first crater depth and first jet height respectively. The second crater depth and second jet height are denoted as κ_2 and δ_2 respectively. Impact sequence generated at Fr = 850. Corresponding video is Movie S1.

from waiting striders. An adult strider exoskeleton including legs has impact area (4) up to $A_s = 165$ mm^2. The water strider legs account for approximately 80% of the impact area, while the torso accounts for approximately 20%. During the heaviest rainfall (50, 51) with drops of mass $m = 16$ mg, falling with an intensity (18) $I \approx 50$ mm/h, a resting adult water strider will experience impacts on average every $\Delta t = m/\rho I A_s \approx 7$ s. Thus, it is highly likely water striders will be struck by drops during rainfall. A snapshot of an oncoming drop relative to a group of resting striders is presented in Fig. 3*A*. We henceforth discuss the subsequent displacement of water striders following drop collision.

Direct Drop Collision Traps Water Strider along Crater Wall. When a drop makes contact with the free surface, liquid is displaced radially such that a crater forms within the body of the liquid bath (30, 52) as pictured in Fig. 3*B*. The low mass of water striders has no measurable effect on splash dynamics nor does the formation of an air bubble around the body of the insect, the plastron. The plastron, shown in Fig. 4, is a survival mechanism sustained by the densely-packed micro- and macro-hairs along the exoskeleton preventing wetting of the strider body. In keeping with the well-established literature on free surface impacts (52), we expect the velocity of expanding craters $U_{c,1}$ to be approximately half the drop impact velocity U. Considering

the limit of impact trials Fr = 850, water striders experience displacement with the expanding crater at velocity $U_{c,1} \approx 3$ m/s which equates to $3 \times$ the characteristic speed of adult striders (4) ~ 1 m/s, and $2 \times$ peak speed ~ 1.5 m/s. Rapid crater expansion
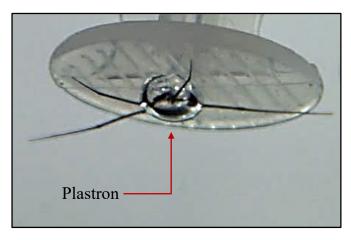

Fig. 4. Plastron forms around the water strider as the syringe plunger pushes the insect beneath the free surface. Densely-packed micro- and macro-hairs populate the water strider's exoskeleton such that water contact angle (21) exceeds 150°. Corresponding video is Movie S3.

debilitates water strider ability to actively resurface, making liquid escape improbable.

Water Striders Are Robust to Forces Imparted by Raindrops.

We posit striders in rainfall experience impact forces comprised of two constituents that are associated with the inertial acceleration of an expanding crater and compression from a decelerating, deforming drop. For our choice of Fr = 127 to 850, initial crater evolution is weakly dependent on the surface tension σ, and viscosity μ of the liquid (53, 54). The time $t = D/U$ represents the time interval between the moment of initial contact of the south pole of a drop with the free surface to the moment at which the north pole of the drop meets the free surface (18, 52). Choosing Fr = 850 such that $t = 0.67$ ms, the maximum inertial force felt by a resting water strider is:

$$F_i = MU_{c,1}/t, \qquad [1]$$

equal to 2.9×10^3 dynes, the equivalent of 483 adult striders, where the weight of a single adult is ~ 6 dynes. We note that all striders struck by a drop atop the free surface survive. As previously stated, there are no measurable changes in the shape and dimension of craters when water striders are present. The volume (55) of a cylindrical adult water strider $\forall_s \approx 7.6$ mm^3 and density $\rho_s = M/\forall_s \approx 850$ kg/m^3 such that $\rho_s/\rho = 0.85$, and thus the strider behaves as a passive liquid parcel along the crater wall. Water striders are subject to reasonably low inertial forces due to their minute mass, akin to the experience of flying insects (18, 19). Unlike flying insects impacted by raindrops, however, drops and the resisting bath impart a normal force that we estimate by considering the impact pressure of the drop. A drop striking the free surface does so with the same impact force as a drop striking a rigid surface with a velocity (53) $U - U_{c,1}$. The related stagnation pressure at the front of the impacting drop is $\rho(U - U_{c,1})^2/2$ and is applied to the strider body area $A_{s,b} = 34$ mm^2, producing a compression force:

$$F_{comp} = \rho(U - U_{c,1})^2 A_{s,b}/2, \qquad [2]$$

equal to 15.3×10^3 dynes, more than $5\times$ greater than the inertial force due to acceleration, F_i. To test the limit of the compression force a strider can withstand, we perform mechanical compression tests (18) using an analytical balance. Water striders are subjected to a sustained compression force and survive up to 150×10^3 dynes, beyond which striders are crippled. Despite the difference in compliance between the water's free surface and the scale's balance pan, our mechanical compression tests give an indication of the strider's ability to survive large compressive loads. Terminal velocity of raindrops, at ~ 9 m/s, will have approximately $2.25 \times$ the kinetic energy $\sim U^2$ of the fastest drops in our tests. At terminal velocities, the strider will experience an increased compressive force $F_{comp} \approx 60 \times 10^3$ dynes, less than half that of the mechanical compression limit of survivability. We conclude a resting water strider atop an aquatic environment is impervious to the forces experienced during raindrop collision.

Water Striders Propelled above the Free Surface by the First Jet.

Now that we have demonstrated the water strider's robustness to

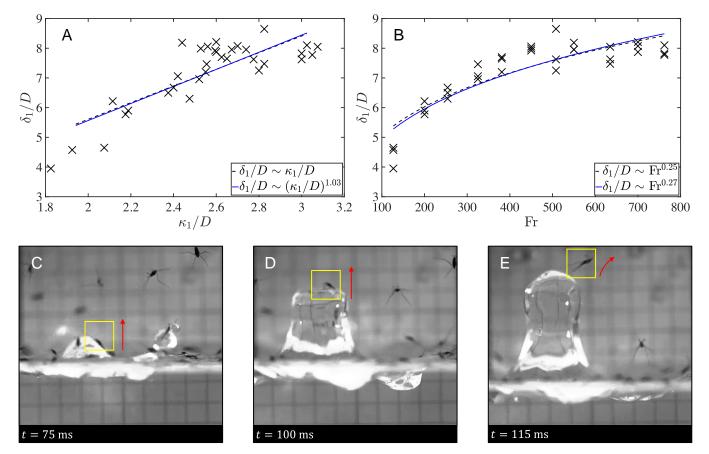**Fig. 5.** (A) Nondimensonalized first jet height δ_1/D versus nondimensonalized first crater depth κ_1/D. (B) Nondimensonalized first jet height δ_1/D versus Froude number. Image sequence showing water strider (C) riding along the first jet, (D) sitting atop the first jet, and (E) jumping from the first jet. Jet generated at Fr ≈ 850. Corresponding video is Movie S4.

forces imparted by impacting raindrops, we turn our attention to the next phases of drop impact. We develop scaling relations that permit us to determine how the principle dimensions of the impact sequence, crater depth and jet height, scale with pre-impact drop properties. Such dimensions culminate in the most critical event in the impact sequence, the collapse of the second crater.

An impact drop pushes the strider into the first crater, as pictured in Fig. 3B. The expanding first crater experiences a buoyant force $F_{B,1} \sim \rho g \forall_{c,1}$, where $\forall_{c,1} \sim D_{c,1}^2 \kappa_1$ is first crater volume, $D_{c,1}$ is first crater diameter, and κ_1 is the crater depth (36). During crater collapse, the water strider rides the first jet super-surface. The collapse of the first crater is dominated by boundary work $W_{B,1} \sim F_{B,1}\kappa_1$, a process in which surface tension σ is negligible for Bond number $Bo = \Delta\rho g \kappa_1^2/\sigma \gg 1$, where $\Delta\rho = (\rho - \rho_a)$ is the difference between water ρ and air density $\rho_a = 1.2$ kg/m^3. As the first crater retracts, the work of the collapsing crater is converted to gravitational potential energy in the jet $W_{B,1} \sim \rho g \forall_{j,1}\delta_1$, where jet volume $\forall_{j,1} \sim D_{j,1}^2 \delta_1$, $D_{j,1}$ is the first jet diameter, and δ_1 is the first jet height. Intuition and experience direct that the diameter of a disturbance in a compliant free surface scales with the diameter of the ensuing response, $D_{c,1} \sim D_{j,1}$. Thus, we may write $\rho g D_{c,1}^2 \kappa_1^2 \sim \rho g D_{j,1}^2 \delta_1^2$. Accordingly, $\delta_1 \sim \kappa_1$. To maintain non-dimensionality,

$$\delta_1/D \sim \kappa_1/D. \qquad [3]$$

Fitting Eq. 3 to experimental data in Fig. 5A produces correlation coefficient $R^2 = 0.69$, while a best fit yields $\delta_1/D \sim (\kappa_1/D)^{1.03}$, $R^2 = 0.69$. Since crater retraction is subjected to boundary work $W_{B,1}$, the expanding first crater is also subjected to the same work (30), and scales with the kinetic energy of the falling drop, $\rho g \forall_{c,1}\kappa_1 \sim \rho D^3 U^2$. Noting that $U^2 = (gD)Fr$, we may write $\kappa_1/D \sim Fr^{1/4}$, and when combined with Eq. 3,

$$\delta_1/D \sim Fr^{1/4}. \qquad [4]$$

We plot δ_1/D vs Fr in Fig. 5B and find Eq. 4 gives a correlation coefficient $R^2 = 0.79$, while a best fit yields $\delta_1/D \sim Fr^{0.27}$, $R^2 = 0.79$.

Eq. 4 may be written as $\delta_1 \sim (UD^{3/2})^{1/2}$ to demonstrate that larger, faster drops produce higher first jets and greater time for the strider to mount an escape from the ongoing impact sequence. Our tests show water strider location on rising jets is a result of their position along the first crater wall. Water striders positioned at the pit of the retracting crater are more likely to ride along the protruding jet to its peak. In our tests, legs often sprawl beyond the jet diameter, making active separation through leg coordination rare. In fact, we observe only one trial where a strider appears to actively separate from the ascending jet by applying a power stroke to the jet mass, causing the insect to be propelled airborne and land outside the impact zone. The singular jet escape sequence is presented in Fig. 5 C–E and Movie S4. Rides on ascending jets pose minimal risks to survival and dryness and serve primarily as a mode of transport between the sub- and super-surface zones. Those striders that do not escape the first jet ride it back below the free surface into the second crater.

Second Craters Eject or Trap Water Striders upon Collapse.

At sufficiently high $Fr \gtrapprox 200$, the momentum of the collapsing first jet produces a more slender, shallower, non-axisymmetric second crater as shown in Fig. 3D. Striders pulled into second craters face
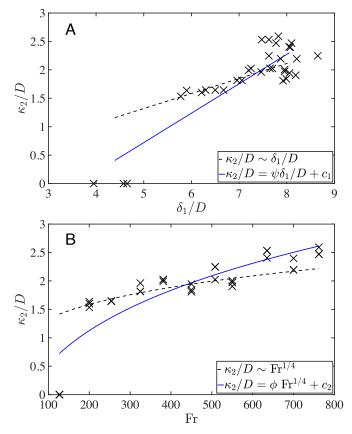

Fig. 6. (A) Nondimensonalized second crater depth κ_2/D versus nondimensonalized first jet height δ_1/D. (B) Nondimensonalized second crater depth κ_2/D versus Froude number.

a greater risk of submersion during second crater collapse than at any other point in the impact sequence of Fig. 3. It is therefore valuable to characterize crater collapse in terms of initial impact conditions when ascribing risk to resting striders.

Consider a water strider trapped along the first jet at the initiation of jet reclination. The water strider will descend below the free surface as gravitational potential energy in the first jet $\rho g D_{j,1}^2 \delta_1^2$ is converted to boundary work for crater expansion $W_{B,2} \sim \rho g D_{c,2}^2 \kappa_2^2$. Given $D_{j,1} \sim D_{c,2}$, we may write,

$$\kappa_2/D \sim \delta_1/D. \qquad [5]$$

Our a priori scaling of second crater depth κ_2/D and first jet height δ_1/D implies first jet ascension to any height above the free surface will lead to second crater formation. Measurements in Fig. 6, however, show that $\kappa_2/D \longrightarrow 0$ for some nonzero δ_1/D, with correlation coefficient $R^2 = 0.60$, thereby revealing a critical first jet height threshold for second crater formation. Therefore, a fit in the spirit of Eq. 5 is done best with an additional fitting constant such that $c_1 < 0$. Hence, Eq. 5 can be recast as:

$$\kappa_2/D = \psi\delta_1/D + c_1. \qquad [6]$$

Fitting Eq. 6 to measurements in Fig. 6A yields best-fit coefficients $\psi = 0.52$, $c_1 = -1.87$, $R^2 = 0.79$, where the negative c_1 value demonstrates that second crater production ceases prior to the full attenuation of the first jet.

Combining Eqs. 4 and 6, we derive:

$$\kappa_2/D = \phi Fr^{1/4} + c_2, \qquad [7]$$

where ϕ and c_2 are best-fit coefficients. Fitting Eq. **7** to measurements in Fig. 6*B* yields $\phi = 0.99$, $c_2 = -2.62$, and $R^2 = 0.76$. Note the poor fit of $\kappa_2/D \sim \mathrm{Fr}^{1/4}$ in Fig. 6*B* ($R^2 = 0.50$). Therefore, water striders are not exposed to second craters for every impact during rainfall since the terminus of some impact sequences is the collapse of a first jet. Faster drops promote deeper second craters which in turn lead to a second subsurface journey for water striders. Going forward, we consider the interaction between striders and collapsing second craters to quantify the dynamics at the threshold of ultimate ejection and entrapment.

Second Crater Acceleration Determines Water Strider Submersion. We note two post-crater scenarios following water strider entanglement with the second crater namely; ejection, and submersion. A side-by-side comparison of the retraction of the first and second craters is presented in Fig. 7 *A* and *B* using image binarization (56, 57) in MATLAB, where λ_1 and λ_2 are widths of the first and second craters, respectively. The spaces between the crater traces of Fig. 7 *A* and *B* show qualitatively precipitous retraction of the second crater compared to the first. To understand the dichotomy presented by the second crater, we consider a critical force F_{sub} required to submerge a water strider resting atop a free surface that accounts for surface tension force at the legs $\sigma\ell$, buoyancy force at the body $g\forall_s(\rho - \rho_s)$, and the weight of the water strider such that:

$$F_{sub} \approx \sigma\ell + g\forall_s(\rho - \rho_s). \qquad [8]$$

A corresponding strider mass $\rho_s\forall_s$ gives a critical acceleration a_{sub} of the free surface above which an average strider will be submerged. Hence, Eq. **8** can be rewritten as:

$$a_{sub}/g \approx [\sigma\ell/\forall_s g + (\rho - \rho_s)]/\rho_s. \qquad [9]$$

Given (4) $\sigma\ell/\forall_s g \gg (\rho - \rho_s)$, where $\mathrm{Ba} = \rho_s\forall_s g/\sigma\ell$, we may write:

$$a_{sub}/g \approx \mathrm{Ba}^{-1}. \qquad [10]$$

Using the mean values for our striders, we estimate $a_{sub}/g \approx 5.7$ [gravities] as a necessary condition for submersion of the water strider by the collapsing second crater in pure water. We choose a representative impact (Movie S5) for analysis at $\mathrm{Fr} \approx 550$ to demonstrate the significance of a_{sub}/g during crater collapse. The retraction of the first crater begins at $\tau = tU/D \approx 41$ and is represented by the crater traces every 0.75 ms in Fig. 7*A*. The colorbar corresponds to the $\Delta\tau$ from when retraction begins. The comparably smaller second crater begins retracting at $\tau \approx 247$. The traces of second crater retraction demonstrate its rapid collapse in Fig. 7*B*. Throughout the retraction of the second crater, we measure the depth of the crater κ_2 for each video frame and the crater width at $y\kappa_2$, where $y = 20, 40, 60,$ and 80%. Study of two-dimensional position data for discrete points along the cavity wall indicates that lateral displacement of the crater-free surface plays a very small part in the magnitude of its acceleration. For simplicity, temporal depth is twice differentiated to provide an acceleration magnitude $a_{c,2}/g$ as the crater collapses. Our differentiation and smoothing technique is provided by Epps et al. (58) which uses a quintic spline to smooth
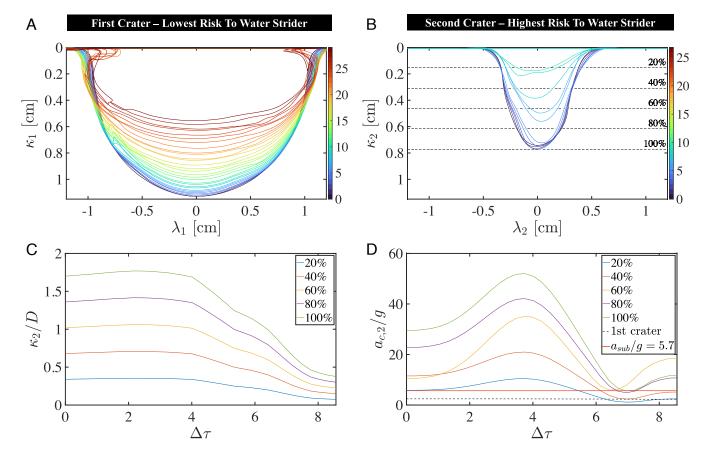

Fig. 7. Crater retraction. Traces of the retraction of the (*A*) first crater, and (*B*) second crater for every $\Delta t = 0.75$ ms. Colormaps indicate $\Delta\tau$ from crater retraction inception. Dimensionless second crater (*C*) depth κ_2/D, and (*D*) acceleration $a_{c,2}/g$ versus dimensionless time from retraction inception $\Delta\tau$. Panel (*D*) contains the $a_{c,1}/g$ curve for the bottom of the first crater for comparison. Craters generated at $\mathrm{Fr} \approx 550$. Corresponding video is Movie S5.

measurements and preserve the physical characteristic of crater evolution as shown in Fig. 7 C and D and $\Delta\tau = 0$ corresponds to the beginning of retraction. The $a_{c,2}/g$ curves of Fig. 7D assume the cavity contracts isometrically, such that a fluid parcel maintains its position relative to the temporal depth of the cavity κ_2. In this example impact, nearly the entire second crater surface experiences $a_{c,2}/g \gtrsim 5.7$, with a peak of > 50 gravities at $\Delta\tau \approx 4$ and at the crater bottom. By comparison, the acceleration at the bottom of the collapsing first crater is minuscule, with a peak < 3 gravities, shown by the dashed curve in Fig. 7D. Different impacts will create second craters that generate more or less acceleration. We, therefore, conclude that the more proximal a water strider is to the bottom point within a second crater the higher the likelihood for crater wall separation from the strider during crater collapse rendering the insect submerged. The threshold for submersion a_{sub}/g will decrease with a decrease in surface tension as in the case of seawater and polluted waterways.

Discussion

Our study demonstrates that small floating organisms can be submerged by impacting drops, but by a different mechanism than intuition may suggest. When water striders retreat below the free surface during second crater formation, we observe ejection for striders positioned within the crater such that $a_{sub}/g < Ba^{-1}$. Both modes of separation from the air–water interface, ejection, and submersion, are attributed to the precipitous retraction of the second craters. While all striders on test are superhydrophobic, we expect hydrophilic particles, even if buoyant, to be more susceptible to submersion because they are less able to separate from jets and more likely to be pulled into the second crater.

Until now, the characterization of second crater dynamics is absent in the literature to the authors' knowledge. We now understand the critical role second craters play in the vertical transport of particles such as floating microplastics, defined as

Fig. 8. (A) Drop impact with the particle-laden free surface. (B) Particle trapped along the crater wall. (C) Particle propelled above free surface by first jet. (D) Particle submerged by second crater. Corresponding video is Movie S6.
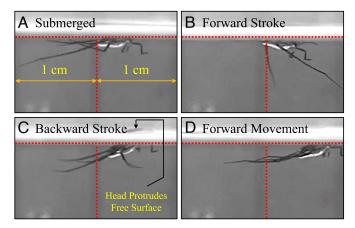

Fig. 9. Underwater locomotion. (A) Resting position below free surface following collapse of the second crater. (B) The water strider rotates legs forward during the first stage of the power stroke. (C) The water strider thrusts legs backward during the second stage of the power stroke. (D) Completed power stroke propels water strider forward. Corresponding video is Movie S7.

plastic debris less than 5 mm in size (47), currently plaguing the world's oceans (48, 49) given that particles experience impact dynamics comparable with water striders, as shown in Fig. 8 and Movie S6. Particles much smaller than water striders have a Ba which is very small and thus have a very high threshold for submersion acceleration, and are candidates for aerosolization by the ejecta of drop impact (20). If not aerosolized, particles too small to be entrapped by raindrops are more susceptible to surface turbulence and diffusion. The transition between the subsurface transport and aerosolization of debris is not yet understood and is an area of future work. Objects considerably larger than striders have a comparatively larger inertia which will influence impact dynamics including crater evolution. Moreover, a larger buoyant force will dominate Eq. **8**.

We present imparted forces in Eqs. **1** and **2** that are seemingly disconnected from drop size D, a form that is inclusive of drops falling from sources other than rain such as waterfalls, tree leaves, and crashing waves. Drops not from rain have impact velocities largely independent of size. If concerned exclusively with rainfall, drop speed is dependent on size and Eqs. **1** and **2** could be written in terms of drop diameter using empirical relations that relate the terminal speed of raindrops to drop diameter (21). We acknowledge our experimental drop impacts are not inclusive of the range of natural rainfall. Less energetic impacts are of little interest and a low threat to striders because of reduced impact forces and reduced likelihood of generating a second crater. More energetic impacts than those tested are likely to be of little danger to striders in the initial stages of impact but will produce deeper second craters such that a larger portion of the crater will generate surface accelerations above Ba^{-1}. We posit impact events onto striders comprised of multiple drops, more probable at higher rainfall intensities, are more likely to leave striders submerged.

Water striders rendered submerged following the second crater collapse are able to survive and locomote below the free surface as illustrated in Fig. 9 and Movie S7. The rapid separation of the second crater from the body of water striders, and repeated impacts from drops reduce the integrity of the plastron in our anecdotal observations. Thus, the exoskeleton of water striders may become saturated such that striders are restricted below the free surface despite being positively buoyant as shown in Fig. 9A. We note water striders' ability to dwell subsurface extends beyond 10 min in some cases.
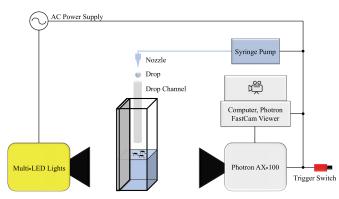
Fig. 10. Schematic of the experimental setup. A Photron Mini AX–100 high-speed video camera captures lateral views of drop collision with diffuse lighting positioned behind the impact chamber. Drops generated from a nozzle affixed to a syringe pump fall through a drop channel to improve chances of direct collision with water striders. Optional trigger switch complements manual controls in video recording software on a computer.

To navigate submergence, striders employ a series of power strokes by first rotating legs forward as shown in Fig. 9*B*, and second, by thrusting legs backward as shown in Fig. 9*C*. These coordinated sequences of leg movements propel water striders upward and forward, and are integral for piercing the free surface but are not always successful in resurfacing, as seen from the failed attempt in Fig. 9*C*, where the head of the water strider pushes against the water line. A powerful stroke and an acute angle of attack at the air–water interface is only one means a strider may employ to reemerge. Floating vegetation may well play a critical role in resurfacing. In the lab, we observe submerged striders take advantage of thin acrylic squares placed in their container at the free surface by gripping the topside of the squares with their legs to aid in resurfacing much like humans crawl onto rafts. The striders rest on the squares to dry and restore the robustness of their hydrophobic exoskeletons. The dynamics of resurfacing and the requirements thereof are a fruitful area for future work.

Methods

Insect Capture and Care. Water striders of non-distinguished age and sex are captured from local ponds, and housed in an $80-cm^2$ tempered-glass aquarium with 16 h of light and 8 h of darkness in keeping with the environmental conditions of the natural habitat. The species of water striders predominantly on test in our study is *Trepobates subnitidus* (59), visually identifiable by an ellipsoidal body shape. Captured water striders demonstrate their typical life processes within the lab, mating, and shedding exoskeletons during maturation. The dwelling environment is maintained at 25 °C ± 2 °C and striders fed dead

mosquitoes. The water bath is kept sanitary using a Cobalt Aquatics Clear Vue underwater filter to prevent the build-up and growth of bacteria. Water strider mass and robustness to mechanical compression forces are measured using a Sartorius Secura 225D–1S analytical balance. Microscopic images are recorded using a Keyence VHX–900F digital microscope.

Impact Trials and Visualization. Water striders are removed from the in-lab aquarium and transferred to a 6-cm wide, 10-cm deep impact chamber affixed to a Nexus 3′ x 6′ optical table. We present a schematic of our experimental setup in Fig. 10. Up to 20 water striders are employed per impact trial covering approximately 22% of the available free surface area which in turn increases the probability of drop collision. Striders are unreplenished for the entire duration of daily experimental trials ~ 1 h. To probe the role of escape jumping during a surface disturbance, we anesthetize water striders with carbon monoxide. We note that unconscious water striders recover on their own when placed atop floating acrylic sheets inside the lab habitat and left undisturbed. A 10-mL syringe connected to a New Era NE–1010 syringe pump is used to generate drops with a constant preset volume flow rate of 5 mL/min, yielding a single drop per impact trial from an elevated nozzle situated 0.3 to 1.7 m above the liquid bath. Given the free reign of water striders, impacts occur opportunistically though drops travel through a drop channel as illustrated in Fig. 10. Collisions are captured with a Photron Mini AX–100 high-speed video camera at 3,200 frames per second with a resolution of 1,280 × 1,024 pixels using a 120-mm Nikon lens. The field of view is 6.5×6.2 cm^2, yielding an 18 pixel/mm magnification. Impacts are illuminated by a pair of 84-watt GS Vitec Multi-LED lights. MATLAB is used to acquire temporal traces and kinematics of craters from captured videos, and the derivative-finding procedure of Epps et al. (58) is employed for acceleration curves. We extract geometric measurements from videos using Open-Source Physics Tracker, and water strider impact area assessments conducted with ImageJ.

Data, Materials, and Software Availability. Raw videos, tabulated data in .xlsx format, MATLAB scripts data have been deposited in Open Science Framework (https://osf.io/xn82j/?view_only=02287dcf89d8430381af27a97 58f37f2) (60).

Author affiliations: [a]Department of Mechanical Engineering, Florida Polytechnic University, Lakeland, FL 33805; [b]Department of Mechanical and Aerospace Engineering, University of Central Florida, Orlando, FL 32816; [c]Department of Bioengineering, Malatya Turgut Ozal University, Malatya 44210, Turkey; and [d]Department of Mechanical, Aerospace, and Biomedical Engineering, University of Tennessee, Konxville, TN 37996

1. N. M. Andersen, J. T. Polhemus, "Water-Striders (Hemiptera: Gerridae, Vellidae, etc.)" in *Marine Insects*, L. Cheng, Ed. (North-Holland Publishing Company, Amsterdam, 1976), pp. 187–224.
2. M. A. Caponigro, C. H. Eriksen, Surface film locomotion by the water strider, Gerris remigis say. *Am. Midl. Nat.* **95**, 268–278 (1976).
3. J. R. Spence, N. M. Anderson, Biology of water striders: Interactions between systematics and ecology. *Annu. Rev. Entomol.* **39**, 101–128 (1994).
4. D. L. Hu, B. Chan, J. W. M. Bush, The hydrodynamics of water strider locomotion. *Nature* **424**, 663–666 (2003).
5. M. Kishi, K. Fujisaki, T. Harada, How do water striders, *Aquarius paludum*, react to brackish water simulated by NaCL solutions? *Naturwissenschaften* **93**, 33–37 (2006).
6. J. W. Bush, D. L. Hu, Walking on water: Biolocomotion at the interface. *Annu. Rev. Fluid Mech.* **38**, 339–369 (2006).
7. G. A. Mahadik *et al.*, Superhydrophobicity and size reduction enabled halobates (insecta: Heteroptera, gerridae) to colonize the open ocean. *Sci. Rep.* **10**, 7785 - (2020).
8. N. M. Andersen, Fine structure of the body hair layers and morphology of the spiracles of semi aquatic bugs insecta hemiptera gerromorpha in relation to life on the water surface. *Vidensk. Meddel. Dansk Naturhist. Foren.* **140**, 7–38 (1977).

9. V. M. Ortega-Jimenez, L. von Rabenau, R. Dudley, Escape jumping by three age classes of water striders from smooth, wavy and bubbling water surfaces. *J. Exp. Biol.* **220**, 2809–2815 (2017).
10. S. Kim, Z. Wu, E. Esmaili, J. J. Dombroskie, S. Jung, How a raindrop gets shattered on biological surfaces. *Proc. Natl. Acad. Sci. U.S.A.* **117**, 13901–13907 (2020).
11. O. Buhler, Impulsive fluid forcing and water strider locomotion. *J. Fluid Mech.* **573**, 211–236 (2007).
12. X. Liang, X. Yao, Y. Zheng, Direction-dependent adhesion of water strider's legs for water-walking. *Solid State Sci.* **14**, 1146–1151 (2012).
13. R. B. Suter, Spider locomotion on the water surface: Biomechanics and diversity. *J. Arachnol.* **41**, 93–101 (2013).
14. W. Yin, Y. L. Zheng, H. Y. Lu, X. J. Zhang, Y. Tian, Three-dimensional topographies of water surface dimples formed by superhydrophobic water strider legs. *Appl. Phys. Lett.* **109**, 1–4 (2016).
15. E. Yang, J. H. Son, S. Lee, P. G. Jablonski, H.-Y. Kim, Water striders adjust leg movement speed to optimize takeoff velocity for their morphology. *Nat. Commun.* **7**, 13698 (2016).
16. H. R. Pruppacher, J. D. Klett, "Microstructure of atmospheric clouds and precipitation" in *Microphysics of Clouds and Precipitation* (Springer, 2010), pp. 10–73.

17. A. F. Spilhaus, Drop size, intensity, and radar echo of rain. *J. Meteorol.* **5**, 161–164 (1948).

18. A. K. Dickerson, P. G. Shankles, N. M. Madhavan, D. L. Hu, Mosquitoes survive raindrop collisions by virtue of their low mass. *Proc. Natl. Acad. Sci. U.S.A.* **109**, 9822–9827 (2012).

19. A. K. Dickerson, P. G. Shankles, L. H. David, Raindrops push and splash flying insects. *Phys. Fluids* **26**, 027104 (2014).

20. M. Lehmann, L. M. Oehlschlägel, F. P. Häusl, A. Held, S. Gekle, Ejection of marine microplastics by raindrops: A computational and experimental study. *Microplast. Nanoplast.* **1**, 1–19 (2021).

21. C. Mätzler, "Drop-size distributions and mie computations for rain" (Research Report No. 2002–16, Institute of Applied Physics, University of Bern, Switzerland, 2002).

22. G.-J. Michon, C. Josserand, T. Séon, Jet dynamics post drop impact on a deep pool. *Phys. Rev. Fluids* **2**, 023601 (2017).

23. F. Rodriguez, R. Mesler, Some drops don't splash. *J. Colloid Interface Sci.* **106**, 347–352 (1985).

24. Y. K. Cai, Phenomena of a liquid drop falling to a liquid surface. *Exp. Fluids* **7**, 388–394 (1989).

25. M. Rein, Phenomena of liquid drop impact on solid and liquid surfaces. *Fluid Dyn. Res.* **12**, 61 (1993).

26. Liow Jong Leng, Splash formation by spherical drops. *J. Fluid Mech.* **427**, 73–105 (2001).

27. S. L. Manzello, An experimental study of a water droplet impinging on a liquid surface. *Exp. Fluids* **32**, 580 (2002).

28. B. Ray, G. Biswas, A. Sharma, Regimes during liquid drop impact on a liquid pool. *J. Fluid Mech.* **768**, 492–523 (2015).

29. M. H. W. Hendrix, W. Bouwhuis, D. van der Meer, D. Lohse, J. H. Snoeijer, Universal mechanism for air entrainment during liquid impact. *J. Fluid Mech.* **789**, 708–725 (2016).

30. M. Artman-Breitung, D. A. Watson, A. K. Dickerson, Simultaneous impact of twin drops on a semi-infinite liquid target. *Phys. Fluids* **33**, 102110 (2021).

31. S. T. Thoroddsen, K. Takehara, The coalescence cascade of a drop. *Phys. Fluids* **12**, 1265–1267 (2000).

32. T. Tran, H. de Maleprade, C. Sun, D. Lohse, Air entrainment during impact of droplets on liquid surfaces. *J. Fluid Mech.* **726**, R3 (2013).

33. G. Agbaglah, S. T. Marie-Jean Thoraval, L. V. Thoroddsen, K. F. Zhang, R. D. Deegan, Drop impact into a deep pool: Vortex shedding and jet formation. *J. Fluid Mech.* **764**, 1–12 (2015).

34. D. A. Watson, J. L. Stephen, A. K. Dickerson, Jet amplification and cavity formation induced by penetrable fabrics in hydrophilic sphere entry. *Phys. Fluids* **30**, 082109 (2018).

35. D. A. Watson, J. L. Stephen, A. K. Dickerson, Impacts of free-falling spheres onto a deep liquid pool with altered fluid and impactor surface conditions. *J. Vis. Exp.* **144**, e59300 (2019).

36. D. A. Watson, C. J. Souchik, M. P. Weinberg, J. M. Bom, A. K. Dickerson, Making a splash with fabrics in hydrophilic sphere entry. *J. Fluids Struct.* **94**, 102907 (2020).

37. J.-S. Koh et al., Jumping on water: Surface tension-dominated jumping of water striders and robotic insects. *Science* **349**, 517–521 (2015).

38. X. Gao, L. Jiang, Water repellent legs of water striders. *Nature* **432**, 36 (2004).

39. X.-Q. Feng, X. Gao, W. Ziniu, L. Jiang, Q.-S. Zheng, Superior water repellency of water strider legs with hierarchical structures: Experiments and analysis. *Langmuir* **23**, 4892–4896 (2007).

40. P. J. Perez Goodwyn et al., Water striders: The biomechanics of water locomotion and functional morphology of the hydrophobic surface (insecta: Hemiptera-heteroptera). *J. Bionic Eng.* **5**, 121–126 (2008).

41. Z.-G. Zhou, Z.-W. Liu, Fabrication of biomimetic water strider legs covered with setae. *J. Bionic Eng.* **6**, 1–6 (2009).

42. A. Balmert, H. F. Bohn, P. Ditsche-Kuru, W. Barthlott, Dry under water: Comparative morphology and functional aspects of air-retaining insect surfaces. *J. Morphol.* **272**, 442–451 (2011).

43. V. Ngo, M. J. McHenry, The hydrodynamics of swimming at intermediate Reynolds numbers in the water boatman (Corixidae). *J. Exp. Biol.* **217**, 2740–2751 (2014).

44. Q. Wang, X. Yao, H. Liu, D. Quéré, L. Jiang, Self-removal of condensed water on the legs of water striders. *Proc. Natl. Acad. Sci. U.S.A.* **112**, 9247–9252 (2015).

45. S. Yewang et al., Nano to micro structural hierarchy is crucial for stable superhydrophobic and water-repellent surfaces. *Langmuir* **26**, 4984–4989 (2010).

46. R. Watanabe, Y. Fujino, T. Yokoi, Predation of frog eggs by the water strider gerris latiabdominis miyamoto (hemiptera: Gerridae). *Entomol. Sci.* **23**, 66–68 (2020).

47. S. Ghosh et al., Microplastics as an emerging threat to the global environment and human health. *Sustainability* **15**, 10821 (2023).

48. J. C. Anderson, B. J. Park, V. P. Palace, Microplastics in aquatic environments. *Environ. Pollut.* **218**, 269–280 (2016).

49. E. Guzzetti, A. Sureda, S. Tejada, C. Faggio, Microplastic in marine organism: Environmental and toxicological effects. *Environ. Toxicol. Pharmacol.* **64**, 164–171 (2018).

50. J. Otis Laws, The relation of raindrop-size to intensity. *EOS Trans. Am. Geophys. Union* **24**, 452–460 (1943).

51. E. Villermaux, B. Bossa, Single-drop fragmentation determines size distribution of raindrops. *Nat. Phys.* **5**, 697–702 (2009).

52. A. Bisighini, G. E. Cossali, C. Tropea, I. V. Roisman, Crater evolution after the impact of a drop onto a semi-infinite liquid target. *Phys. Rev. E* **82**, 036319 (2010).

53. E. Berberović, N. P. van Hinsberg, S. Jakirlić, I. V. Roisman, C. Tropea, Drop impact onto a liquid layer of finite thickness: Dynamics of the cavity evolution. *Phys. Rev. E* **79**, 036306 (2009).

54. T. T. Truscott, B. P. Epps, J. Belden, Water entry of projectiles. *Annu. Rev. Fluid Mech.* **46**, 355–378 (2013).

55. D. J. Fairbairn, Allometry for sexual size dimorphism: Testing two hypotheses for Rensch's rule in the water strider *Aquarius remigis. Am. Nat.* **166**, S69–S84 (2005).

56. J. J. Schoppink et al., Cavitation-induced microjets tuned by channels with alternating wettability patterns. *Phys. Fluids* **35**, 032017 (2023).

57. M. E. Alif, J. Veihdeffer, M. E. Alam, Liquid jet stability through elastic planar nozzles. *Eur. Phys. J. Spec. Top.* **232**, 827–835 (2023).

58. B. P. Epps, T. T. Truscott, A. H. Techet, "Evaluating derivatives of experimental data using smoothing splines" in *Proceedings of Mathematical Methods in Engineering International Symposium, MMEI, Lisbon Portugal* (Polytechnic Institute of Coimbra, Portugal, 2010).

59. P. D. Kittle, Water striders (hemiptera: Gerridae) of Arkansas. *J. Arkansas Acad. Sci.* **34**, 68–71 (1980).

60. D. A. Watson et al., Water striders are impervious to raindrop collision forces and submerged by collapsing craters. Open Science Framework. https://osf.io/xn82j/?view_only= 02287dcf89d8430381af27a9758f37f2. Deposited 12 November 2023.